Dynamic Modeling of a Rotating Insect Wing

Mark Jankauski*, I.Y. Shen
University of Washington, 371 Loew Hall, Seattle, WA 98195

ABSTRACT

A dynamic model of an insect wing is developed treating the wing as a deformable body subject to three-dimensional finite rotation about a fixed point at the base of the wing. Discretization of a stationary wing is conducted via finite element analysis to determine the natural frequencies and mode shapes of the wing. By formulating and discretizing the kinetic and potential energy, we derive the equation of motion governing the modal response of a flapping wing using Lagrange's equation. The equation of motion indicates Coriolis, Euler, and centrifugal forces resulting from the finite rotation are responsible for the wings elastic deformation. Numerical integration reveals a beat phenomenon that arises from the Coriolis excitation in the first vibration mode. The beat phenomenon is insensitive to yaw amplitudes and non-zero initial conditions but diminishes in the presence of damping. The beat phenomenon can potentially be used to estimate gyroscopic forces.

1 INTRODUCTION

Insect flight has recently been a subject of significant research within biology and engineering communities. For biologists, such studies provide critical insights into the sensorimotor coordination of movement in animals. For example, knowledge of the instantaneous wing shape helps determine the direction and magnitude of aerodynamic forces acting upon the wing. This leads to an understanding of lift-to-drag ratio, thrust production and aerodynamic efficiency of insect flight [1, 2]. Moreover, wing deformation activates strain receptors (mechanosensation cells), which provides the insect brain with feedback used to identify flight status. Insect wings are richly imbued with strain sensors [3].

For engineers, insect flight research can help realize autonomous flying objects, such as flapping-wing micro-aerial vehicles (MAVs). Flapping-wing MAVs are capable of performing difficult maneuvers and stationary hovering while consuming relatively little power [4]. These characteristics are desirable for indoor flight, and consequently have generated interest in potential military surveillance and reconnaissance applications [5]. While several MAVs have been successfully developed, there remains a necessity for design optimization in order to reduce weight, power consumption, and cost [6]. A functional dynamic wing model may facilitate this effort.

Several models have previously been developed to describe the complex dynamics of an insect wing during flight. Many kinematic and dynamic models treat the insect body and wings as several connected rigid bodies. For example, a kinematic model developed by Roccia et al. treats the wing as a rigid body subject to three-dimensional rotation about a fixed point on the insect body [7]. An alternative dynamic model developed by Orlowski and Girard also treats the insect forewing as a rigid body, and considers aerodynamic loading as a generalized force acting on the wing [8]. Such kinematic and dynamic models can be used to effectively estimate wing velocity and aerodynamic force production while retaining a lower number of degrees of freedom. However, by treating the wing as a rigid body, such models are unable to provide information about localized strains, and therefore have limitations in determining insect neural feedback or designing strain-based control systems for MAVs.

Alternatively, researchers have developed finite element analysis (FEA) based models [9]. Finite element models are capable of estimating localized strains on a deformed wing for each mode shape. However, FEA models are limited to infinitesimal rotation and cannot describe the entire time-dependent strain response of a flapping wing. The large rigid body motion and rotation of the wing generate a time-varying stiffness matrix $\mathbf{K}(t)$. The implication of this is that the wing will have to be re-meshed during each time step of the analysis, resulting in a larger number of degrees of freedom. The significant number of degrees of freedom makes a direct FEA model computationally impractical. Physical insights, such as the contribution of gyroscopic forces, may also be lost.

Each of these models is capable of independently describing aspects of insect flight, such as aerodynamic force production and strain. However, there remains a necessity to unify these models such that all their positive attributes can be fully realized. By synthesizing characteristics from each of these models, we develop in this paper a reduced-order model of a flapping insect wing with the following important characteristics. First, the model is capable of predicting strain components under finite rotation. Second, the model retains a low order to maintain computational feasibility, thereby facilitating parametric studies. Third, the model can accommodate nonspecific geometry and therefore can be used to describe any flapping insect wing. Lastly, the model discretizes the wing via finite element analysis, so arbitrary geometry can be implemented readily. As a first attempt at model formulation,

*Email address:mjankaus@uw.edu

effects of aerodynamics and aeroelasticity are neglected. It is assumed elastic deformation of the wing is solely a result of inertial-elastic effects [2].

The remainder of the paper is organized as follows. First, the dynamic model is formulated using Lagrange mechanics. The model is then applied to a *Manduca sexta* forewing, revealing a beat phenomenon in the first two modes caused by the interaction of gyroscopic and centrifugal forces with the free vibration of the wing. Various factors that may affect the presence of the beat phenomenon are then investigated, including initial conditions, yaw rotation amplitude, and damping.

2 Formulation

The model assumes the wing as a deformable body subject to three-dimensional rotation about a point fixed on the insect's body. The displacement of any point on the wing is described by two finite rotations (pitch and roll), one small rotation (yaw), and one infinitesimal out-of-plane deflection. The rigid body displacement of the wing is a kinematic process, and can readily be determined by establishing a rotating coordinate frame. The out-of-plane deflection is characterized as a dynamic process, and must be calculated by solving the equations of motion derived through potential and kinetic energy terms.

2.1 Kinematics

The wing is placed into a fixed reference frame, with the origin representing the fixed point of rotation and I, J, K being three orthogonal unit vectors associated with the fixed reference frame. (Fig 1). For the purposes of this formulation, I, J, K will also be referred to as coordinate axes. A rotating reference frame that pitches and rolls but does not yaw with the wing is established. The first rotation (roll) has an amplitude α and occurs about the I-axis, transforming the reference frame to the $I^{'} - J^{'} - K^{'}$ coordinate system. The second rotation (pitch) has an amplitude of β and occurs about the $J^{'}$-axis, transforming the reference frame to the $I^{''} - J^{''} - K^{''}$ coordinate system. Both of these rotations are assumed to have large and finite amplitudes. The third rotation corresponds to the yaw rotation, and is denoted by γ. The yaw rotation (Figure 2) is assumed small, and therefore small angle approximations are employed. Consequently, the yaw rotation is not considered in the rotating reference frame. Through simple geometric analysis, the angular velocity $\vec{\Omega}$ of the rotating coordinate frame $I^{''} - J^{''} - K^{''}$ is:

$$\vec{\Omega} = \dot{\alpha} cos\beta I^{''} + \dot{\beta} J^{''} + \dot{\alpha} sin\beta K^{''} \tag{1}$$

With the rotating coordinate frame established, a position vector $\vec{R}_n$ (Fig 2) is drawn in the $I^{''} - J^{''} - K^{''}$ reference frame from the point of rotation to a differential mass dm on the wing geometry. $\vec{R}_n$ is the sum of three intermediate position vectors, $\vec{r}_1, \vec{r}_2$, and $\vec{r}_3$ (i.e., $\vec{R}_n = \vec{r}_1 + \vec{r}_2 + \vec{r}_3$), where $\vec{r}_1$ represents the position of the differential mass without yaw,

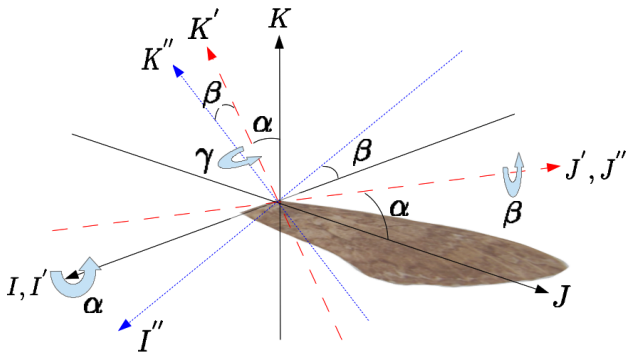

Figure 1: Development of a rotating reference frame

$\vec{r}_2$ represents the contribution of the yaw rotation to the position, and $\vec{r}_3$ represents the out-of-plane elastic deformation of the wing. In-plane deformation is assumed to be small, and is neglected in this formulation. Specifically, $\vec{r}_1, \vec{r}_2$, and $\vec{r}_3$ are described in both Cartesian and cylindrical coordinates as follows:

$$\vec{r}_1 = xI^{''} + yJ^{''} = r\vec{e}_r \tag{2}$$

$$\vec{r}_2 = \gamma(-yI^{''} + xJ^{''}) = \gamma r\vec{e}_\theta \tag{3}$$

$$\vec{r}_3 = W(\vec{r}_1, t)K^{''} = W(\vec{r}_1, t)\vec{e}_z \tag{4}$$

Above, x and y are the coordinates of the differential mass and $W(\vec{r}_1, t)$ is the elastic deformation dependent on both time and position. The position vector $\vec{R}_n$ can then be differentiated with respect to time to determine the velocity of the differential mass. As dm is in a rotating coordinate frame, the chain rule must be applied to account for the time derivative of the coordinate frame. The resulting expression for the differential mass velocity $\dot{\vec{R}}_n$ is:

$$\dot{\vec{R}}_n = \vec{\Omega} \times \vec{R}_n + \dot{\vec{r}}_2 + \dot{\vec{r}}_3 \tag{5}$$

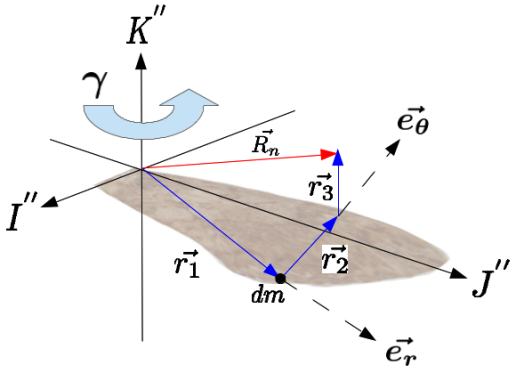

Figure 2: Position vectors and yaw rotation

2.2 Kinetic and Potential Energies

The kinetic energy T of the wing is

$$T = \frac{1}{2}\int_m \dot{\vec{R}}_n \cdot \dot{\vec{R}}_n \, dm \tag{6}$$

where Equation 6 is integrated over the domain of the wing. The potential energy V is

$$V = \frac{1}{2}\int_v S(W,W)dv \tag{7}$$

where $S(W,W)$ represents a quadratic and symmetric strain energy density function, i.e., $S(a,b) = S(b,a)$, and the domain of integration is the volume of the wing. The use of the strain energy density function allows this formulation to be applied for any elastic body with complex geometry.

2.3 Discretization

The unknown deformation of the wing $W(\vec{r}_1,t)$ can be expressed via an eigenfunction expansion

$$W(\vec{r}_1,t) = \sum_{k=1}^{\infty} \phi_k(\vec{r}_1)q_k(t) \tag{8}$$

where $\phi_k(\vec{r}_1)$ is the k^{th} mode shape and $q_k(t)$ is its modal response to be determined. Moreover, the mode shapes $\phi_k(\vec{r}_1)$ are normalized with respect to the mass satisfying the following orthonormal conditions,

$$\int_m \phi_k \phi_e \, dm = \delta_{ke} \tag{9}$$

where δ_{ke} is the Kronecker delta. Similarly, $\phi_k(\vec{r}_1)$ experiences orthogonality via the strain energy density function,

$$\int_v S(\phi_k,\phi_e)\, dv = \omega_k^2 \, \delta_{ke} \tag{10}$$

where ω_k is the natural frequency of the k^{th} mode shape. The advantage to the eigenfunction expansion is that the mode shape $\phi_k(\vec{r}_1)$ and the natural frequency ω_k may be determined using finite element modeling. Therefore, this formulation is valid for any arbitrary wing shape. Moreover, the boundary conditions of the wing are accounted for directly in the finite element analysis, and need not be evaluated explicitly for development of the equations of motion.

Two geometric vectors useful to the derivation of the equations of motion are defined as follows

$$\vec{a}_k = \int r\phi_k(\vec{r}_1)\vec{e}_r dm = \int \phi_k(xI^{''} + yJ^{''})dm \tag{11}$$

$$\vec{b}_k = \int r\phi_k(\vec{r}_1)\vec{e}_\theta dm = \int \phi_k(-yI^{''} + xJ^{''})dm \tag{12}$$

where $\vec{a}_k$ represents a geometric vector corresponding to the position of the inertial force center of the k^{th} mode shape relative to the point of rotation, and $\vec{b}_k$ (Equation 12) represents a 90° counter-clockwise rotation from $\vec{a}_k$.

2.4 Equation of Motion

To develop the equations of motion, kinetic and potential energy terms are discretized via Equation 8 and then subjected to Lagrange's equation. The modal response of the k^{th} mode, $q_k(t)$, is the generalized coordinate. The resulting equation of motion is determined as

$$\ddot{q_k} + [w_k^2 - (\dot{\alpha}^2 cos^2\beta + \dot{\beta}^2)]q_k = \\ -\dot{\vec{\Omega}} \cdot (\gamma\vec{a_k} - \vec{b_k}) - (K^{''} \cdot \vec{\Omega})[\vec{\Omega} \cdot (\vec{a_k} + \gamma\vec{b_k})] - 2\dot{\gamma}\vec{\Omega} \cdot \vec{a_k} \tag{13}$$

Equation 13 is a linear, time-varying second order ordinary differential equation. Time-variance is introduced in the stiffness coefficient, $[w_k^2 - (\dot{\alpha}^2 cos^2\beta + \dot{\beta})]$, and is a direct result of centrifugal softening. Forcing terms appear on the right hand side of Equation 13 as a result of the wing's rotation. Interestingly, three forces typical in rotating coordinate frames are identified: the Coriolis force, Euler force, and centrifugal force. Each of these forces has a corresponding vector projection that is described in terms of $\vec{a_k}$ and $\vec{b_k}$. Table 1 shows the vector projection of each forcing term specific to the wing.

Forcing Term	Projected Representation
Euler Force	$-\dot{\vec{\Omega}} \cdot (\gamma\vec{a_k} - \vec{b_k})$
Centrifugal Force	$-(K^{''} \cdot \vec{\Omega})[\vec{\Omega} \cdot (\vec{a_k} + \gamma\vec{b_k})]$
Coriolis Force	$-2\dot{\gamma}\vec{\Omega} \cdot \vec{a_k}$

Table 1: Summary of Excitation Terms

Due to the linearity of Equation 13, solutions for $q_k(t)$ may be determined independently for each forcing term outlined in Table 1. This result is meaningful, as it allows direct comparison between the generalized coordinate response $q_k(t)$ for each type of force.

3 EXAMPLE

To demonstrate the usage of Equation 13, the proposed model is applied to the forewing of the hawkmoth *Manduca sexta*. The *Manduca sexta* is an ideal subject for insect flight study due to the small variation between individual specimens and the abundance of available research [10]. To apply Equation 13, a finite element model is constructed to determine the mode shapes and natural frequencies of a *Manduca sexta* forewing. Next, assumed rotation profiles are presented for the insect in forward flight. The excitation terms and generalized coordinate responses for the first two mode shapes are then analyzed. Finally, the effects of initial conditions, yaw

rotation amplitudes, and damping on generalized coordinate responses are explored.

3.1 Finite Element Modeling

Finite element modeling is used to find mode shapes and natural frequencies of the wing. Published research has determined the natural frequencies and mode shapes of the *Manduca sexta* forewing via finite element analysis, and the results agree closely with experimental results [11]. These finite element models serve as a benchmark for the finite element model developed for this research.

A to-scale finite element model of the wing is constructed in ABAQUS by tracing computed tomography (CT) images of a *Manduca sexta* forewing. A camber of approximately 13% of the wing chord length is implemented, and has the notable effect of providing support to the first bending mode. Due to the aspect ratio of the wing, shell elements are utilized. Venation patterns of a real *Manduca sexta* forewing are neglected, and paper material is used in lieu of the actual membrane material. The properties of the paper used in the finite element model are given in Table 2.

Symbol	Description	Value	Units
t	Thickness	81	μm
E	Young's Modulus	10	MPa
ρ	Density	0.86	g/cm^3
ν	Poisson's Ratio	0.3	-

Table 2: Assumed material properties for the finite element paper wing

The natural frequencies determined by the finite element model are shown in Table 3, and the corresponding mode shapes are shown in Figure 3. The natural frequencies of the first two mode shapes agree within 4.5% of the reported values, indicating that the paper wing can adequately describe the dynamics of an actual *Manduca sexta* forewing.

Natural Frequency	Determined Value	Reported Value
ω_1	62.5 Hz	60 Hz
ω_2	86.9 Hz	84 Hz

Table 3: Comparison of paper wing natural frequencies and reported *Manduca sexta* natural frequencies [11]

Vectors $\vec{a}_k$ and $\vec{b}_k$ are then determined numerically from the mode shapes pictured in Figure 3 using the following approximation.

$$\vec{a}_k = \sum_{i=1}^{j} \phi_{i,k}(x_i, y_i)[x_i I'' + y_i J'']dm_i \qquad (14)$$

$$\vec{b}_k = \sum_{i=1}^{j} \phi_{i,k}(x_i, y_i)[-y_i I'' + x_i J'']dm_i \qquad (15)$$

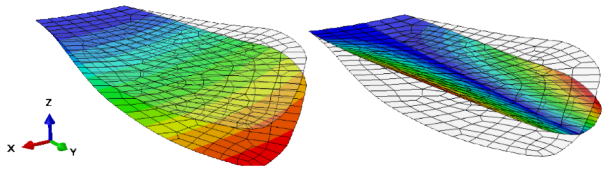

Figure 3: First two mode shapes of the paper wing- (Left) First Spanswise Bending, (Right) First Spanwise Torsion

Above, the i index denotes the i^{th} node of the finite element model and the j index represents the total number of nodes. Therefore, x_i and y_i represent the $x-y$ coordinates of the i^{th} node, $\phi_{i,k}(x_i, y_i)$ represents the k^{th} mode shape of the i^{th} node, and dm_i represents the nodal mass of the i^{th} node. Table 4 shows the geometric vectors $\vec{a}_k$ and $\vec{b}_k$ for the first two modes. In general, $\vec{a}_k$ and $\vec{b}_k$ are very small. Therefore, a second set of vectors $\vec{a}'_k$ and $\vec{b}'_k$ is defined, where $\vec{a}'_k$ and $\vec{b}'_k$ are normalized with respect to the largest component of vectors $\vec{a}_k$ and $\vec{b}_k$. For predictions of physical quantities (i.e., strain distribution), $\vec{a}_k$ and $\vec{b}_k$ will be used. For comparison of modal responses, $\vec{a}'_k$ and $\vec{b}'_k$ will be used due to the convenience of their magnitudes.

Vector	I''	J''
$\vec{a}_1$	0.7552×10^{-5}	0.0934×10^{-5}
$\vec{b}_1$	-0.0934×10^{-5}	0.7552×10^{-5}
$\vec{a}_2$	-0.1728×10^{-5}	-0.0033×10^{-5}
$\vec{b}_2$	0.0033×10^{-5}	-0.1728×10^{-5}

Table 4: Geometric Vectors for first two mode shapes- Paper Wing FEA model

3.2 Rotation Profiles

Equation 13 allows for any function to describe pitch, roll, and yaw rotations independently. In this example, each rotation is assumed sinusoidal and periodic with a frequency of ω_d representing the flap frequency of the *Manduca sexta*. Mathematically, the roll rotation takes the form $\alpha = \alpha_0 \sin(\omega_d t)$, where α_0 denotes the rotation amplitude in radians. The pitch and yaw rotations take the same form, with their amplitudes described by β_0 and γ_0 respectively. Phase angles are not considered in this example.

The flight of the *Manduca sexta* is divided into two principal regimes— forward flight and hovering flight. In each of these regimes, rotation amplitudes α_0, β_0 and γ_0 exhibit vastly different characteristics. Typical rotation amplitudes for a *Manduca sexta* traveling forward at a speed of 5 m/s are shown in Table 5 [10]. For this example, only the forward flight regime is considered. The flapping frequency used is $\omega_d = 25$ Hz, which falls within the observed 24.8-26.5 Hz range of flap frequencies [10].

Rotation Parameter	Amplitude (rad)
α_0	0.8
β_0	0.5
γ_0	0.2

Table 5: Rotation Amplitudes for Forward Flight (5 m/s) [10]

3.3 Time/Frequency Domain of System Parameters

Each of the system parameters is investigated in time and frequency domains. The system parameters correspond to the time-varying stiffness and excitation terms of Equation 13. Figure 4 shows each of the system parameters as a function of time for the first mode shape.

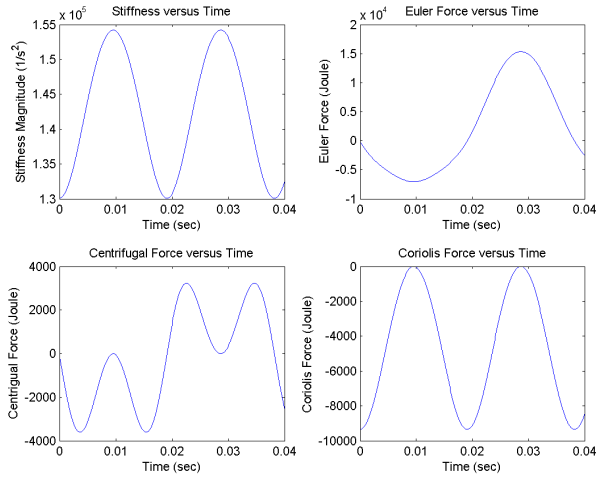

Figure 4: Systems Parameters in the time domain- First mode shape

From Figure 4, it can be seen that the Euler Force has the largest magnitude, the Coriolis Force has the second largest magnitude, and the centrifugal force has the smallest magnitude. Both the stiffness and Coriolis force vary nearly sinusoidally in sync with a frequency of approximately twice the flap frequency. The Euler and centrifugal forces appear to have more complicated forms. To determine the frequency content of each of these system parameters, a power spectral density (PSD) algorithm is employed.

The PSD decomposes each of the system parameters into its frequency components. The Coriolis Force and stiffness oscillate at a frequency close to $2\omega_d$. The Centrifugal force oscillates predominately at $3\omega_d$, with sub harmonics occurring at ω_d. The Euler force oscillates at ω_d, with super harmonics occurring at $2\omega_d$, $3\omega_d$, etc. In this case, super harmonics $3\omega_d$ and above tend to have a negligible effect. Oscillation frequencies of the Coriolis force occur near the first natural frequency ω_1, and oscillation frequencies of the centrifugal force occur near the second natural frequency ω_2. The proximity to natural frequencies may have a marked effect on the generalized coordinate responses.

3.4 Generalized Coordinate Responses

Equation 13 is solved assuming zero initial conditions (e.g. $q_k(0) = 0, \dot{q}_k(0) = 0$). The response subject to each excitation term is solved individually, and due to linearity, the results are summed to determine the overall system response. In this section, all responses are solved numerically using Matlab. The results for the first mode are shown in Figure 5.

The generalized coordinate responses for the first mode provides interesting results. First, despite having the largest magnitude, the Euler force generates only the second largest response. The Euler force generates oscillations predominately at a frequency ω_d, roughly half the natural frequency of the first mode ω_1. On the other hand, the Coriolis force oscillates at $2\omega_d$, which is close to ω_1. As a result, the Coriolis force generates a larger response due to operating near resonance despite having a lesser magnitude than the Euler force.

Second, a clear beat phenomenon exists in the Coriolis response. The beat phenomenon occurs between the $2\omega_d$ oscillation frequency of the Coriolis force and effective natural frequency ω_1 of the first mode shape. Lastly, the centrifugal force appears to have a very minor contribution to the response of the first mode shape. This is due to the relatively low magnitude of the centrifugal force coupled with the fact that dominant oscillations occur away from the first natural frequency.

Next, the response of the second mode shape is solved. Similar to the Coriolis force for the first mode shape, the centrifugal force oscillates near the second natural frequency ω_2. The result is a significant contribution to the generalized coordinate response, as well as the presence of a beat phenomenon occurring between $3\omega_d$ and the effective natural frequency of the second mode shape. Both the Euler force and Coriolis force oscillate away from resonance, and therefore have comparatively low contributions to the response.

4 Beat Phenomenon

Numeric simulations indicate the beat phenomenon occurs in the first and second modes as a response to Coriolis and centrifugal forcing, respectively. Such a response is a result of the forced vibration interacting with the free vibration of the wing. The beat phenomenon as revealed can also be used as a way to detect gyroscopic forces. The beat amplitude is proportional to the yaw amplitude γ_0. It remains an open question as to how insects detect gyroscopic forces. The beat phenomenon, both in frequency and magnitude, may potentially allow insects to detect such gyroscopic forces.

Frye hypothesizes that the frequency content generated by the stretch receptor in the *Manduca sexta* forewing plays a vital role in the neural feedback used by the insect to interpret flight status [12]. It seems plausible then that the beat phenomenon has biological significance in providing neural

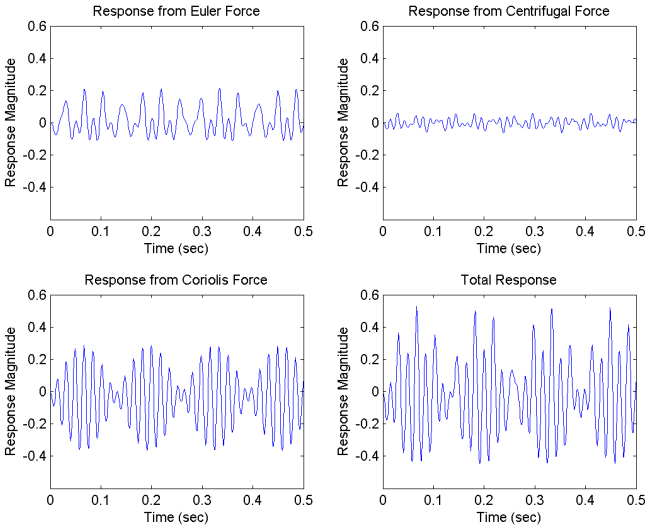

Figure 5: Generalized Coordinate Responses to Excitation Terms- First Mode

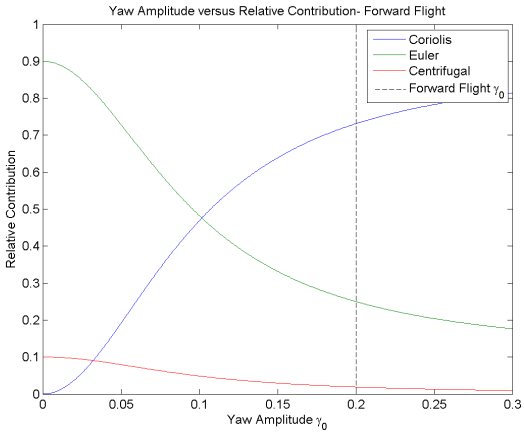

Figure 6: Relative Contribution of Forcing terms to Response as a function of γ_0

feedback during insect flight. As the total generalized coordinate response exhibits a beat response, the strain components in the wing will also reflect a beat response. Should the insect be capable of interpreting beat effects in the first two modes, the rotations α,β and γ may be identified. As these rotations have a direct correlation to aerodynamic parameters (e.g. lift, drag), the beat amplitudes may be used to identify flight status. Consequently, it is possible that MAV design could implement strain-based control systems rather than accelerometer-based control systems. This may potentially reduce both the weight and the power consumption of the MAV. Motivated by the potential applications of the beat phenomenon, we determine the sensitivity of the beat response in the first mode subject to Coriolis forcing.

4.1 Sensitivity to Yaw Amplitude

The amplitude of the yaw rotation, γ_0, has been found to have a tremendous influence on the magnitude of the Coriolis force. While the typical yaw amplitudes for forward flight (Table 5) are relatively consistent, individual specimens may deviate slightly from these values. Therefore, the contribution of each forcing term to the wing response is determined as a function of γ_0. To remain consistent with the small angle approximation, a range of yaw amplitude $0 \leq \gamma_0 \leq 0.3$ is considered. Equation 13 is solved independently for the Coriolis, Euler and centrifugal forces over the entire range of γ_0 assuming zero initial conditions (e.g. $q_k(0) = 0, \dot{q}_k(0) = 0$). The square sum of each partial response is divided by the square sum of the total response to determine the contribution of each forcing term as a percentage. The results of the simulation are shown in Figure 6.

At the operation point of γ_0 described in Table 5, the contribution of the Coriolis force to the total response is substantially larger than the contribution from the other two forces. In the forward flight regime, even large variations of γ_0 will cause only a minor change in the Coriolis contribution. Thus, an increase of γ_0 results in the amplification of the beat phenomenon. This study also shows the beat phenomenon can serve as an effective way to obtain $\dot{\gamma}$ from the wing response.

4.2 Sensitivity to Initial Conditions

The beat phenomenon results from an interaction between the forced vibration of the Coriolis force and the free vibration of the wing. From a purely mathematical standpoint, there exists a set of initial conditions that will cause the free vibration of the wing to disappear from the response. If there is no free vibration of the wing to interact with the forced vibration, the beat phenomenon will no longer be present.

Consequently, it is prudent to look at the Coriolis contribution as a function of non-zero initial conditions. To identify an allowable set of initial conditions, Equation 13 is solved assuming zero initial conditions. For the forward flight regime, the maximum and minimum values of $q(t)$ and $\dot{q}(t)$ constitute the upper and lower bounds of allowable initial conditions. Mathematically, this takes the form $q(t)_{min} \leq q(0) \leq q(t)_{max}$ and $\dot{q}(t)_{min} \leq \dot{q}(0) \leq \dot{q}(t)_{max}$. The Coriolis contribution is then determined by solving Equation 13 over the entire set of initial conditions using the time-dependent formulation. The results are shown in Figure 7.

Figure 7 shows the contribution of the Coriolis force is more than 60% for most initial conditions. Even for extreme initial conditions, the contribution of the Coriolis force still constitutes about 33% of the total contribution. Thus, some non-zero initial conditions may cause the beat phenomenon to become less distinct, but it will never entirely be removed from the total response.

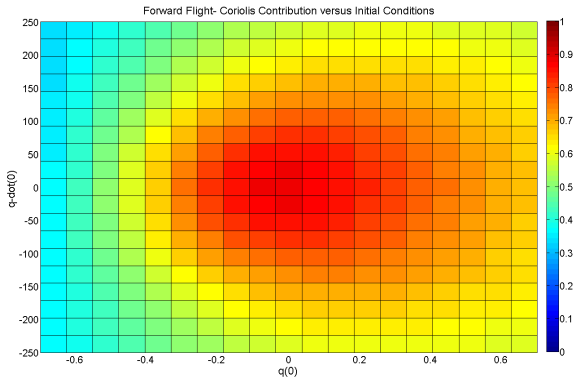

Figure 7: Relative Contribution of Coriolis Response to Various Initial Conditions

4.3 Damping

As the beat phenomenon relies partially on the free vibration of the wing, structural damping may have the effect of diminishing the beat over time. To determine the significance of these effects, structural damping of 1% ($\zeta = 0.01$) is introduced into Equation 13. The response subject to Coriolis forcing is then determined numerically for the first mode shape (Figure 8). As the free vibration of the wing dissipates as a result of damping, the beat phenomenon gradually becomes less pronounced. After several seconds, the Coriolis force causes only the forced vibration of the wing, which oscillates sinusoidally at $2\omega_d$.

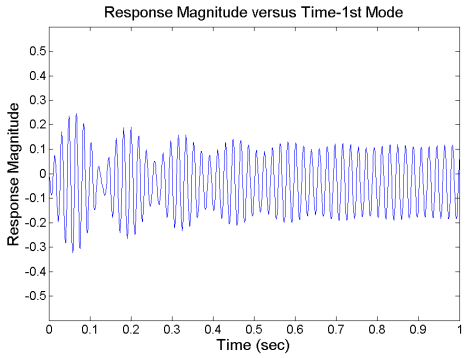

Figure 8: Damped generalized coordinate response to Coriolis forcing, First mode

For insects, there exist a number of ways in which the beat phenomenon may be preserved in the response in spite of structural damping. First, rotation amplitudes may be randomized slightly from their mean values to better represent flapping of a real insect. Subtle variations, particularly in the yaw amplitude, allow the beat phenomenon to be maintained. Second, the insect may perform an aerial maneuver, corresponding to both a considerable change in rotation amplitudes and an abrupt translation of the insect body. Both of these factors can cause free vibration to occur, thereby reestablishing the beat phenomenon. This suggests that it is desirable for an insect to move frequently to preserve neural feedback generated by deformation of the forewings.

4.4 Strains

Consider a point of interest on the wing $P(x, y)$. Let ϵ_x be the normal strain in the x-direction, ϵ_y be the normal strain in the y-direction, and τ_{xy} be the shear strain in the xy plane at $P(x, y)$. The strain components can be represented by

$$\epsilon_x(x, y, t) = \sum_{k=1}^{\infty} \epsilon_{x,k}(x, y) q_k(t) \tag{16}$$

$$\epsilon_y(x, y, t) = \sum_{k=1}^{\infty} \epsilon_{y,k}(x, y) q_k(t) \tag{17}$$

$$\tau_{xy}(x, y, t) = \sum_{k=1}^{\infty} \tau_{xy,k}(x, y) q_k(t) \tag{18}$$

where $\epsilon_{x,k}$ is the normal strain in the x-direction of the k^{th} mode, $\epsilon_{y,k}$ is the strain in the y-direction of the k^{th} mode, and $\tau_{xy,k}$ is the shear strain in the xy plane of the k^{th} mode. The first mode is a spanwise bending mode, resulting in significant strain at the center of the wing base. The second mode is a spanwise torsion mode, and results in large strains at the leading and trailing edge of the wing base.

A point $P(x, y)$ is selected near the base of the wing. The strain components are determined by finite element analysis for the first two mode shapes as shown in Table 6.

Strain component	First Mode ϕ_1	Second Mode ϕ_2
ϵ_x	256	-161
ϵ_y	-1577	96.7
τ_{xy}	691	1710

Table 6: Strain components normalized with respect to mass matrix for first two modes at $P(x, y)$

$q_1(t)$ and $q_2(t)$ are calculated by numerically solving Equation 13 assuming zero initial conditions and using the $\vec{a}_k$ and $\vec{b}_k$ vectors. The total time-dependent strain is determined using the strain values from Table 6 and applying Equations 16-18. The results are shown in Figure 9. The shear strain τ_{xy} has the largest magnitude, while the x-component of strain ϵ_x and the y-component of strain ϵ_y have comparatively negligible magnitudes. For all strain components, the beat phenomenon is observed.

5 Conclusion

A comprehensive dynamic model of an insect wing is developed treating the wing as a deformable body subject to three dimensional rotation about a fixed point on the insect's body. A coordinate frame that rotates with the finite pitch

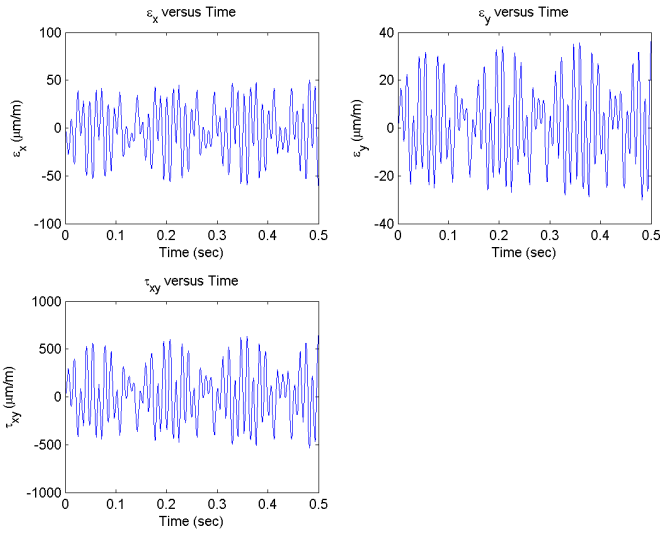

Figure 9: Time dependence of strain components at $P(x, y)$

and roll rotations is established. The yaw rotation is assumed small, and is allowed to rotate independently of the coordinate frame. The kinetic and potential energies are formulated, and the set of uncoupled differential equations describing the time response of each mode shape (determined by finite element analysis) is determined by Lagrange's equation. There are several advantages to such a formulation. First, the model is able to estimate the time-dependent strain components on the wing. Second, the model allows any complex geometry to be implemented readily. Third, the resulting model has reduced order— the order of the model is the number of mode shapes retained.

The model is then applied to the forewing of the *Manduca sexta*. Coriolis, Euler, and centrifugal forces are identified excitation terms responsible for the elastic deformation of the wing. The Coriolis force tends to dominate the first mode whereas the centrifugal force tends to dominate the second mode. Numerical integration indicates a beat phenomenon occurs in both the first and second modal responses. The sensitivity of the beat phenomenon in the fundamental mode is explored. The beat phenomenon is relatively insensitive to various yaw amplitudes and non-zero initial conditions, but decays gradually in the presence of damping. Resetting of initial conditions or slight variations of the yaw amplitude cause the beat phenomenon to persist even in the presence of damping.

The total time-dependent normal and shear strain components are calculated at a point of interest near the base of the wing. The shear strain component is determined to be significantly larger than the normal strain components. In all cases, the strain components exhibit a beat phenomenon. This result suggests the *Manduca sexta* may use strain frequency data associated with the beat phenomenon to help identify flight status. In the context of MAVs, similar strain-based control systems may be developed to replace or supplement traditional accelerometer-based control systems. This can potentially increase MAV performance by reducing weight, size, and power consumption.

6 References

[1] *An Introduction to Fluid Dynamics*. Cambridge, 1967.

[2] T.L. Daniel and S.A. Combes. Into thin air: contributions of aerodynamic and inertial-elastic forces to wing bending in the hawkmoth manduca sexta. *The Journal of Experimental Biology*, 2003.

[3] Ron Galant, James B. Skeath, Steve Paddock, David L. Lewis, and Sean B. Carroll. Expression pattern of a butterfly *achaete-scute* homolog reveals the homology of butterfly wing scales and insect sensory bristles. *Current Biology*, 1998.

[4] R.C. Michelson and S. Reece. Update on flapping wing micro air vehicle research. In *Proceedings of 13th Bristol International RPV Conference*.

[5] Adam P. Tobias. *Experimental methods to characterize nonlinear vibration of flapping wing micro air vehicles*. PhD thesis, Air Force Institute of Technology, 2007.

[6] R.J. Wood. Liftoff of a 60mg flapping-wing mav. In *Intelligent Robots and Systems*.

[7] Bruno A. Roccia, Sergio Preidikman, Julio C. Massa, and Dean T. Mook. Development of a kinematical model to study the aerodynamics of flapping-wings. *International Journal of Micro Air Vehicles*, 2011.

[8] Christopher T. Orlowski and Anouck R. Girard. Modeling and simulation of nonlinear dynamics of flapping wing micro air vehicles. *AIAA Journal*, 2011.

[9] Satish K. Chimakurthi and Carlos E. S. Cesnik. Flapping-wing structural dynamics formulation basedon a corotational shell finite element. *AIAA Journal*, 2011.

[10] Alexander P. Willmott and Charles P. Ellington. The mechanics of flight in the hawkmoth manduca sexta. *The Journal of Experimental Biology*, 1997.

[11] Aaron G. Norris, Anthony N. Palazotto, and Richard G. Cobb. Experimental structural dynamic characterization of the hawkmoth (manduca sexta) forewing. *International Journal of Micro Air Vehicles*, 2013.

[12] Mark A. Frye. Encoding properties of the wing hinge stretch receptor in the hawkmoth manduca sexta. *The Journal of Experimental Biology*, 2001.